Study of the confined Ising magnet with long-range competing boundary fields

2005 J. Phys.: Condens. Matter 17 4579

(http://iopscience.iop.org/0953-8984/17/29/001)

INSTITUTE OF PHYSICS PUBLISHING JOURNAL OF PHYSICS: CONDENSED MATTER

J. Phys.: Condens. Matter **17** (2005) 4579–4604 doi:10.1088/0953-8984/17/29/001

Study of the confined Ising magnet with long-range competing boundary fields

Andres De Virgiliis[1,2], Ezequiel V Albano[1,2], Marcus Müller[2,3] and Kurt Binder[2]

[1] Instituto de Investigaciones Fisicoquímicas Teóricas y Aplicadas (INIFTA), UNLP, CONICET. Casilla de Correo 16, Sucursal 4, (1900) La Plata, Argentina
[2] Institut für Physik, Johannes Gutenberg Universität, Staudingerweg 7, D-55099 Mainz, Germany
[3] Department of Physics, University of Wisconsin-Madison, 1150 University Avenue, Madison, WI 53706-1390, USA

Received 31 March 2005, in final form 20 June 2005
Published 8 July 2005
Online at stacks.iop.org/JPhysCM/17/4579

Abstract

We present extensive Monte Carlo simulations of the Ising film confined in an $L \times M$ geometry ($L \ll M$) in the presence of long-range competing magnetic fields $h(n) = h_1/n^3 (n = 1, 2, \ldots, L)$ which are applied at opposite walls along the M-direction. Due to the fields, an interface between domains of different orientations that runs parallel to the walls forms and can be located close to one of the two surfaces or fluctuate in the centre of the film (localization–delocalization transition). This transition is the precursor of the wetting phase transition that occurs in the limit of infinite film thickness ($L \to \infty$) at the critical curve $T_w(h_1)$. For $T < T_w(h_1)$ ($T \geqslant T_w(h_1)$) such an interface is bound to (unbound from) the walls.

We study this transition by measuring the magnetization profiles across the sample and the distribution function of both the magnetization of the whole sample and that of the centre of the film as a function of temperature, T, or strength of the wall field, h_1. We obtain estimates of the size-dependent wetting *'critical'* points that allow us to extrapolate to the thermodynamic limit. Using the results of these extrapolations, confirmed by independent measurements of the cumulant, we draw the phase diagram of the wetting transition with long-range surface fields.

We show that, starting from a localized interface well inside the non-wet phase, the position of the interface diverges exponentially when approaching the transition point, in contrast to the power-law divergence observed in the case of short-range fields.

The properties of the delocalized interface are also studied. Within the wet phase the width of the capillary waves broadens the observed interface profiles. The spectrum of capillary waves is cut off at large wavelengths by the correlation length, $\xi_\parallel$, which scales like $\xi_\parallel \sim L^2$, similar to the short-range case. Additionally, the interface stiffness is obtained from the Fourier spectrum of the capillary waves.

1. Introduction

Let us consider a confined system below its bulk critical temperature ($T_{c,b}$) where several phases can coexist. The interaction with the confining walls may favour a phase different from the phase prevailing in the bulk, and this fact may lead to the growth of a wetting layer at the walls, separated by an interface from the bulk phase [1–6]. The study of wetting phenomena of solid surfaces by a fluid has attracted much attention not only for the interesting phase behaviour with several types of phase transition [7–32], but also because it is of primary importance for many technological applications (lubrication, efficiency of detergents, oil recovery in porous materials, stability of paint coatings, interaction of macromolecules with interfaces, etc [1, 35–37]).

Wetting transitions are also observed when a magnetic material is in contact with a wall where a surface magnetic field acts. For example, let us consider an Ising ferromagnet [38, 39] with positive magnetization in the bulk and in the absence of any bulk magnetic field. Here, a negative boundary field h_1 acting at the wall at a certain temperature T may stabilize a domain of negative magnetization at the surface, separated from the bulk by an interface. In the non-wet state of the wall the thickness of the wetting layer is microscopically small (of the order of few lattice spacings) and the interface is said to be bound to the wall. However, by a suitable change of the control parameters, such as T and h_1, the system may undergo a wetting transition, where the thickness of the wetting layer diverges. Of course, if the system is confined between two walls which are placed L lattice spaces apart, such a divergence becomes rounded off. However, the interface is no longer bound to any wall and becomes delocalized. This localization–delocalization transition is the precursor of a true wetting transition that occurs in the semi-infinite system [40]. It is worth mentioning that a large number of studies of the confined Ising magnet have been reported in the literature; see e.g. [9–11, 13, 16, 17, 40, 42–51].

The aim of this paper is to present and discuss extensive Monte Carlo simulations of the critical wetting for the confined two-dimensional Ising model in the $L \times M$ geometry, considering long-range magnetic fields acting at the walls which run along the M-direction. Most of the available studies on wetting transitions in the Ising magnet are restricted to short-range fields, stimulated by the existence of exact results, at least in some limiting cases [53, 40, 67–69]. However, it is known [53, 2, 3, 66] that long-range surface forces modify the wetting behaviour significantly, and in fact for many physical applications the choice of long-range forces would be more realistic [9, 10, 59] than their short-range counterparts.

Such long-range boundary fields can be described by a power-law decay of the field with the distance n to the wall, $h(n) = h_1\, n^{-p}$, where p is a suitable exponent. We consider only the case $p = 3$ here, since this choice is the physically most relevant case for fluids interacting with an attractive wall (remember that the Ising magnet can be considered, in the framework of the lattice gas interpretation, as a lattice model of the gas–liquid transition). Integrating over all the van der Waals interactions between a (semi-infinite) wall and a fluid atom, e.g. integrating the attractive part of a Lennard-Jones potential (decaying with distance r as r^{-6}) over all atoms of the wall, one obtains an n^{-3} interaction. Also from a theoretical point of view in $d = 2$ dimensions the case $p = 3$ is most interesting [62] (remember that in an effective interface Hamiltonian description $h(n)$ translates into an interface potential $V(\ell) \sim l^{-\delta}$ with $\delta = p - 1$, ℓ being the distance of the interface from the wall [1–5]). It turns out that $p = 3(\delta = 2)$ is a borderline case: for $p > 3$ the entropic repulsion of the interface dominates $V(\ell) \sim k_B T \ell^{-2}$ [65], and the wetting behaviour is asymptotically the same as in the case of short-range surface fields; however, for $p < 3$ one would obtain exponents at complete wetting that depend on p [62]. For the case $p = 3$ and critical wetting, however, an exponential divergence of the correlation lengths describing interfacial fluctuations

approaching the wetting transition has been predicted [62], which does not occur for other values of p.

In a previous numerical work [31] we have addressed the question of the influence of long-range boundary fields on the wetting behaviour of the Ising magnet. These studies aimed at understanding the behaviour of both the magnetization profiles across the film and the correlation function [31] along the film. For these purposes it was not necessary to attempt to accurately locate the critical points along the wetting curve, which is not known exactly yet, in contrast to its short-range counterpart [40]. In fact, as already remarked [31], due to computational limitations we were unable to perform reliable extrapolations of the finite-size estimates for the critical points to the thermodynamic limit. This shortcoming is overcome in this paper, where we increase the statistics by more than one order of magnitude. In this way, extrapolating to the thermodynamic limit, we have located four points of the wetting phase transition line, that, in addition to two points known trivially, provide a reliable overview of the phase diagram. By means of a suitable location of the interface position along the strip, we have access to the probability distribution of these local fluctuations. From this function we obtain, in turn, the mean position, the width and the correlation length of the interface. These quantities are then compared to estimates extracted from the analysis of the magnetization profiles and the spin–spin correlations. The results obtained by these independent methods are found to be in good qualitative agreement, and provide evidence for the exponential divergence of the relevant length scales upon approaching the critical point. The influence of a bulk magnetic field on the critical behaviour of the system is also addressed. We find a power law divergence in the limit of a vanishing field within the wet phase (complete wetting). Furthermore, a detailed study of the properties of the delocalized interface and its dependence on the film thickness is presented. Using capillary wave theory we evaluate the interfacial stiffness. The comparison with results previously obtained for the case of short-range fields allows us to identify the influence of the long-range nature of the fields on the wetting behaviour of the confined system.

The paper is organized as follows: after a short description of the theoretical background (section 2), techniques and results are then presented and discussed in section 3, while the conclusions are summarized in section 4.

2. Theoretical background

2.1. The confined Ising ferromagnet magnet with long-range boundary fields

We consider an Ising ferromagnet on the square lattice with a Hamiltonian given by

$$\mathcal{H} = -J \sum_{\langle i,j \rangle} S_i S_j - h \sum_i S_i - \sum_n h(n) \sum_{i \in n} S_i, \tag{1}$$

where J is the nearest-neighbour coupling, the sum $\langle i, j \rangle$ is extended once over all nearest neighbour bonds, and h is a (bulk) uniform field that acts on all spins and is measured in units of J.

We have used a $L \times M$ geometry with periodic boundary conditions in the x-direction (where the system has the linear dimension M), and free boundary conditions in the z-direction, where we label successive layers by the index n, and apply competing, long-range surface fields $h(n)$ at the free boundaries [9–11]

$$h(n) \equiv h_1[n^{-3} - (L - n + 1)^{-3}] \qquad n = 1, \ldots, L \tag{2}$$

where h_1 is the magnitude of the surface magnetic field that is measured in units of the coupling constant J.

The Ising magnet in two dimensions and in the absence of any external magnetic field undergoes a second-order order–disorder transition when the temperature is raised from a relatively low initial value. The critical temperature of this model is known exactly, $k_B T_{c,b}/J = 2/\ln(1+\sqrt{2}) = 2.269\ldots$ [39, 52]. In the following, temperatures are reported in units of $T_{c,b}$. On the other hand, in the presence of competing surface fields the formation of an interface between magnetic domains of opposite directions running along the film is observed. In this confined geometry, such an interface undergoes a localization–delocalization transition (as the temperature is raised keeping h_1 constant). This behaviour of the interface is the precursor of the wetting phase transition that occurs in the thermodynamic limit. We note that for the case of short-range surface fields the wetting critical curve has been calculated exactly [40], yielding

$$\exp(2J/k_B T)\cdot[\cosh(2J/k_B T) - \cosh(2h_{1c}/k_B T)] = \sinh(2J/k_B T), \qquad (3)$$

where k_B is the Boltzmann constant and $h_{1c}(T)$ is the critical surface field (the inverse function of the wetting temperature $T_w(h_1)$). However, for long-range fields the phase diagram is not known exactly yet, except for two extremal points, namely for $T = 0 h_1 = [\sum_{n=1}^{\infty} n^{-3}]^{-1}$ [31], while for $T = 1 h_1 = 0$.

The field given by equation (2) is equivalent, in the thermodynamic limit, to an effective interface potential of the type [62, 63]

$$V(\ell) \sim h\ell - \frac{B}{\ell^2}, \qquad (4)$$

where ℓ is the distance of the interface to the wall, h is the bulk field, and $B \sim h_1$ denotes the strength of the surface field. In the framework of the theory of wetting, this kind of potential is marginal between the *strong* and the *weak* fluctuation regimes [64]. Also, this effective potential is of the order of the *effective* entropic repulsion in $d = 2$ dimensions [65, 66]

$$V_{fl} \sim k_B T \ell^{-2}. \qquad (5)$$

Therefore, when approaching the wetting transition and in the thermodynamic limit $L \to \infty$, the relevant length scales diverge according to [63]

$$\xi_\parallel \sim \xi_\perp^2 \sim \langle\ell\rangle^2 \sim \xi_0 \exp(b(T_w - T)^{-1/2}), \qquad (6)$$

$\xi_\perp$ and $\xi_\parallel$ being the correlation lengths perpendicular and parallel to the film walls, respectively. The divergence given by equation (6) resembles the Kosterlitz–Thouless transition [60], where the enthalpy of the vortex–antivortex pair at a distance ℓ scales as $J \ln \ell$, and the entropy scales as $T \ln \ell$. In fact, in the present case, the enthalpy of the interface at a distance ℓ from the wall scales as $-h_1 \ell^{-2}$ and the entropy scales as $T\ell^{-2}$, so that the energy and the entropy of the relevant degree of freedom scale in the same way with the length [31].

In the presence of a bulk magnetic field h, and at a fixed temperature $T > T_w(h_1)$, the divergence of these lengths upon approaching bulk coexistence, $h = 0$, obeys power laws with universal exponents [57]

$$\langle\ell\rangle \sim \xi_\perp \sim \xi_\parallel^{1/2} \sim h^{-1/3}. \qquad (7)$$

This means that $\beta^{co} = \nu_\perp^{co} = 1/3$, $\nu_\parallel^{co} = 2/3$, and the index co stands for 'complete wetting'.

In view of these results, let us now briefly review the scaling theory for critical wetting with long-range fields as given by equation (2) [11, 31]. The singular part of the surface free energy for a film of thickness L and length M can be written as

$$f_s = \xi_\parallel^{-1} \tilde{F}_s(L\xi_\parallel^{-1/2}, M\xi_\parallel^{-1}, h\xi_\parallel^{3/2}) \qquad (8)$$

where $\tilde{F}(X, Y, Z)$ is a scaling function. Despite the fact that equation (6) formally implies $\nu_\parallel = \infty$ and $\nu_\parallel/\nu_\perp = 2$, we make use of the scaling argument that M scales with $\xi_\parallel$ and L scales

with $\xi_\perp$ to motivate equation (8). Now in order to locate the localization–delocalization transition of the interface in a film with constant M/L^2, we take $X = 1$ (for $Z = 0$) in equation (8). Defining $t \equiv (T_w - T)/T_w$ as the scaled temperature variable, one finds

$$X = L\xi_\parallel^{-1/2} = 1, \qquad \xi_\parallel^c = L^2, \tag{9}$$

and obtains

$$t_c(L) \sim (\ln L)^{-2}, \qquad T_{c,L} - T_w \sim (\ln L)^{-2}. \tag{10}$$

Equation (10) can be utilized to extrapolate the finite size estimate of the wetting critical temperature extracted from the Monte Carlo simulations to the thermodynamic limit. It should be noted that now $T_{c,L}$ is more strongly depressed from T_w with decreasing L than in the case of short-range fields, where $T_{c,L} - T_w \propto L^{-1}$.

Then we proceed to discuss the scaling properties for some of the thermodynamic functions that can be derived from equation (8). The surface excess magnetization is given by

$$m_s \equiv \left(\frac{\partial f_s}{\partial h}\right)_{T,h_1} = \xi_\parallel^{1/2}\tilde{m}_s(L\xi_\parallel^{-1/2}, M\xi_\parallel^{-1}, h\xi_\parallel^{3/2}) \tag{11}$$

where $\tilde{m}_s$ is another scaling function. One can recognize from this equation that $m_s \sim \xi_\perp$. Hence this quantity will be applied in our calculations as an independent measure of the perpendicular correlation length of the film. We have for $t = 0$ in the limit $L \to \infty$ (but $M/L^2 =$ constant)

$$m_s \sim h^{-1/3}\hat{m}_s(M/L^2), \tag{12}$$

in agreement with equation (7). The surface susceptibility becomes

$$\chi_s \equiv \left(\frac{\partial m_s}{\partial h}\right)_{T,h_1} = \xi_\parallel^2\tilde{\chi}_s(L\xi_\parallel^{-1/2}, M\xi_\parallel^{-1}, h\xi_\parallel^{3/2}) \tag{13}$$

where $\tilde{\chi}_s$ is another scaling function. The *total* susceptibility of the system can be split into bulk and surface contributions as

$$\chi = \chi_b + \frac{1}{L}\chi_s \approx \frac{1}{L}\chi_s, \qquad t \to 0 \tag{14}$$

where the last approximation results from the fact that χ_b exhibits a non-singular behaviour in the vicinity of the wetting transition. Taking in equation (13) the limit $h = 0$ and keeping M/L^2 fixed, a finite maximal value of χ must be reached for a constant value of the scaling variable $t \sim 1/(\ln L)^2$, because χ cannot be divergent for a system which is finite in all its extensions. This maximal value is given by

$$\chi^{\max} \sim \frac{\xi_\parallel^2}{L} \sim L^3, \tag{15}$$

where we have used the relationship $\xi_\parallel \sim L^2$, from equation (9). This equation in turn implies that the fluctuation of the bulk magnetization at $t = 0$ is of order unity, cf equation (27) below.

On the other hand, the confined interface can also be treated in terms of the capillary wave Hamiltonian given by

$$\mathcal{H}[\ell] = \int_0^M \mathrm{d}x \left\{\frac{\Gamma}{2}\left[\frac{\mathrm{d}\ell(x)}{\mathrm{d}x}\right]^2 + V[\ell(x)]\right\}, \tag{16}$$

where Γ/k_BT is the interfacial stiffness and $V(\ell)$ is an effective potential acting on the interface position due to the confining walls. Within a mean-field framework, it is expected that $\ell(x)$ would weakly fluctuate so that $V(\ell)$ can be expanded around the mean position

$\bar{\ell} = L/2$ [16, 54]. Using this approximation, neglecting constant terms and defining $u(x) \equiv \ell(x) - L/2$, one obtains

$$\mathcal{H}[u] = \int_0^M \mathrm{d}x \left\{ \frac{\Gamma}{2}\left[\frac{\mathrm{d}u(x)}{\mathrm{d}x}\right]^2 + \frac{1}{2}\left(\frac{\partial^2 V}{\partial \ell^2}\right)_{u=0} u^2 \right\}. \tag{17}$$

Taking the Fourier components of the local interface position $u(x)$ and using the equipartition theorem, one obtains for the mean square value of the component $u(q)$ [4, 3]

$$\langle |u(q)|^2 \rangle^{-1} = \beta\Gamma(q^2 + \xi_\parallel^{-2}) \tag{18}$$

where the parallel correlation length for interfacial fluctuations is given by

$$\xi_\parallel^{-2} = \frac{1}{\Gamma}\left(\frac{\partial^2 V(\ell)}{\partial \ell^2}\right)_{u=0}. \tag{19}$$

In order to obtain a reliable estimation of the dependence of $\xi_\parallel$ on L one has to consider that the fluctuations of the interface create, at a distance ℓ from the wall, an effective entropic repulsive potential given by equation (5) [65, 66]. Then, replacing equation (5) in the mean field equation (19), one obtains

$$\xi_\parallel \sim L^2. \tag{20}$$

This result is also in agreement with the predictions of the transfer matrix method given, for short-range wall potentials, by

$$\xi_\parallel = \frac{2\beta\Gamma}{3\pi^2} L^2, \tag{21}$$

and with scaling arguments [16]. For the sake of completeness, let us also recall that for the case of short-range wall potentials the same result (equation (21)) can be obtained by means of the solid-on-solid (SOS) approach applied to Ising films [51, 53].

Furthermore, replacing the obtained relationship for $\xi_\parallel$ in the expression of the Fourier spectra (equation (18)), it is possible to evaluate the mean square displacement of the interface for a finite value of M as follows:

$$s^2 \equiv \langle u^2(x) \rangle = \sum_q \langle |u(q)|^2 \rangle = \frac{M}{2\pi} \int_{2\pi/M}^{2\pi/a} \mathrm{d}q \, \langle |u(q)|^2 \rangle \tag{22}$$

where a is a short-wavelength cut-off (usually of the order of the lattice spacing). Now using equation (18), one gets

$$s^2 = \frac{\xi_\parallel}{2\pi\Gamma}\left[\tan^{-1}\left(\frac{2\pi\xi_\parallel}{a}\right) - \tan^{-1}\left(\frac{2\pi\xi_\parallel}{M}\right)\right]. \tag{23}$$

Since we are interested in the limit $\xi_\parallel \gg a$ it is possible to use the approximation $\tan^{-1}(2\pi\xi_\parallel/a) \approx \pi/2$. Also, for $\xi_\parallel \ll M$ one can use $\tan^{-1}(x) \approx x$ in the second term, so one has

$$s^2 \approx \frac{\xi_\parallel}{4\Gamma}\left(1 - 4\frac{\xi_\parallel}{M}\right), \qquad \xi_\parallel \ll M. \tag{24}$$

Now, combining equations (20) and (24), it follows that

$$s^2 \sim L^2, \tag{25}$$

and the width of the interfacial profile is of the same order as the thickness of the strip.

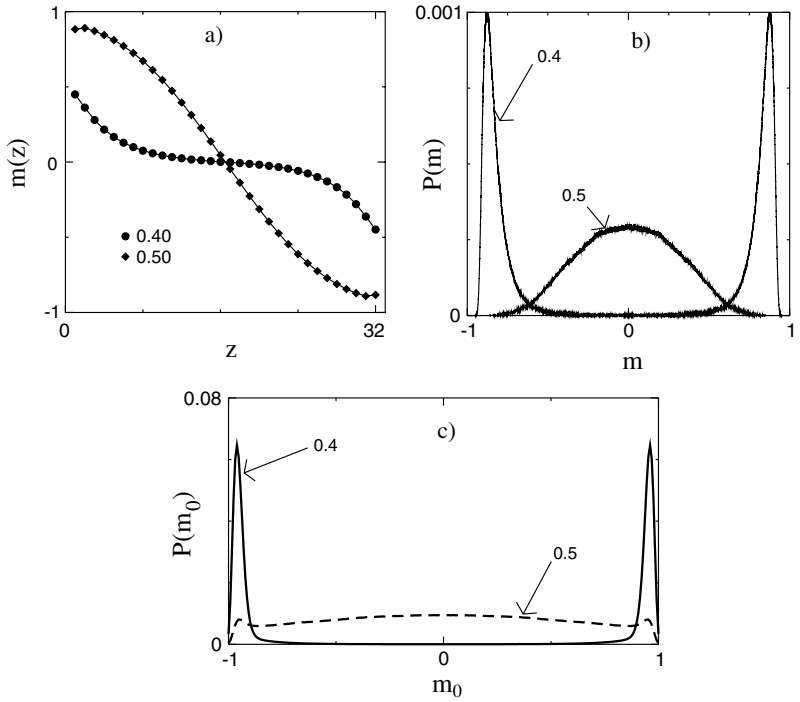

Figure 1. Set of typical plots describing the interface localization–delocalization transition in an Ising film of size $L = 32$ and $M = 256$, where long-range surface magnetic fields are applied. Data correspond to $T = 0.8$ and two different values of h_1, as listed in the figures. (a) Magnetization profiles $m(z)$. (b) Distribution function of the total magnetization m. (c) Distribution function of the magnetization at the centre of the film, m_0.

3. Results and discussion

3.1. Brief details on the Monte Carlo simulation method

Simulations are performed using lattices of width $L = 12$, 16, 24, 32, and 48, and taking $M = L^2/4 = 36$, 64, 144, 256, and 576, respectively. The standard Metropolis algorithm is used in all simulations. Typical runs are performed with 10^6–4×10^6 MCSs, disregarding the first 10^5–4×10^5 MCSs for equilibration, where during each Monte Carlo time step (MCS) an attempt is made to flip $L \times M$ spins of the sample once on average. Results are averages over four to eight independent runs, depending on the lattice size.

3.2. The wetting phase diagram

In order to gain insight into the behaviour of the model it is useful to first discuss an overview of the dependence of some relevant observables on both the surface field and the temperature. To this purpose we have fixed the temperature at $T = 0.8$, while the magnitude of the surface field is changed. We show here the magnetization profiles across the film ($m(z)$, see figure 1(a)), the distribution function of the magnetization of the thin film ($P(m)$, see figure 1(b)) and the distribution function of the magnetization along the centre of the film ($P(m_0)$, where $m_0 \equiv m(z = L/2)$, see figure 1(c)).

It is found that for the smallest value of the field ($h_1 = 0.4$) $P(m)$ exhibits a double-peaked structure (the peaks are located close to values of the spontaneous magnetization of the

unconfined system, as shown in figure 1(b)). This result is the typical fingerprint of a localized interface within the *non-wet* phase, showing the coexistence of two equivalent states, each of them with a non-zero average magnetization. In such states the interface is bound to one of the walls of the film. The distribution $P(m_0)$ also exhibits two sharp peaks (figure 1(c)). Additionally, the shape of the magnetization profile is also consistent with the presence of two coexisting phases (figure 1(a)) [16].

On the other hand, for $h_1 = 0.5$ one finds that the interface is delocalized so that the system is in the *wet* phase. In fact, the distribution $P(m)$ is now a Gaussian centred around $m = 0$, while $P(m_0)$ also exhibits a single peak at $m_0 = 0$. This scenario is consistent with the presence of an interface performing excursions across the film and placed, on average, along the centre of the sample. Consequently, the profile $m(z)$ exhibits a typical sigmoidal shape which corresponds to this *soft mode* phase.

Now we describe the different quantities that were analysed in this study. After recording the distribution function of the magnetization for samples of different sizes and scanning conveniently both T and h_1, it is possible to analyse the behaviour of the system by evaluating the moments of the distribution. The first moment simply gives the average magnetization m of the thin film

$$\langle |m| \rangle = \frac{\int_0^1 m P(m)\, \mathrm{d}m}{\int_0^1 P(m)\, \mathrm{d}m}, \tag{26}$$

while the susceptibility is given by the following relationship:

$$k_\mathrm{B} T \chi = LM(\langle m^2 \rangle - \langle |m| \rangle^2). \tag{27}$$

In addition, we have calculated the fourth-order cumulant given by

$$U_L = 1 - \frac{\langle m^4 \rangle}{3\langle m^2 \rangle^2}, \tag{28}$$

which has proven very useful for the location of critical points [61].

As done in many other studies of interfaces in lattice models, the magnetization profiles across the film were also employed in the present work:

$$m(z) \equiv \frac{1}{M} \sum_{x=1}^{M} S(x, z). \tag{29}$$

Additionally, the surface layer magnetization

$$m_1 = \frac{1}{2M} \left(\sum_{x=1}^{M} S(x, z = 1) - \sum_{x=1}^{M} S(x, z = L) \right) \tag{30}$$

and susceptibility

$$\chi_{11} \equiv \frac{\partial m_1}{\partial h(1)} = M[\langle m_1^2 \rangle - \langle m_1 \rangle^2], \tag{31}$$

where $h(1)$ is a field that acts only in the surface layer were recorded. These quantities play an important role in the theory of surface critical phenomena [34].

Finally, from the magnetization profiles we can also obtain the surface excess magnetization, given by

$$m_\mathrm{s} = \sum_{z=1}^{L/2} (m_b - m(z)) \tag{32}$$

and noting that for large $zm(z)$ must approach the bulk magnetization in the film, m_b.

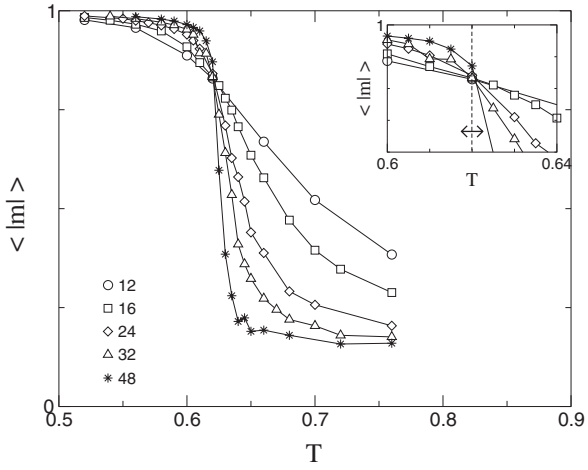

Figure 2. Plots of the magnetization $|m|$ versus T as obtained keeping $h_1 = 0.6$ constant and using lattices of different sizes as shown in the figure. The inset shows a detailed view of the intersection point of the curves corresponding to samples of different sizes. The double arrow gives an estimate of the error involved in the determination of the intersection point.

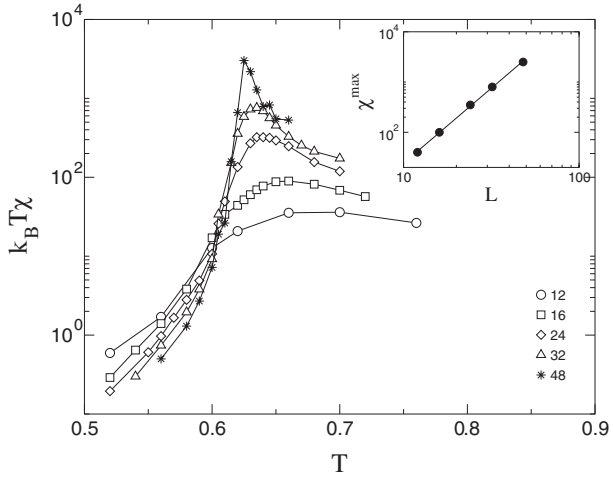

Figure 3. Plots of the susceptibility versus T as obtained keeping $h_1 = 0.6$ constant and using lattices of different sizes as shown in the figure. The inset shows the size dependence of the maximum of the susceptibility $k_B T \chi^{max}$. The straight line shows the fit $\chi^{max} \sim L^3$.

Figures 2–4 show the temperature dependence of the total magnetization, the susceptibility and the cumulant obtained for a fixed surface field $h_1 = 0.6$ and using samples of different sizes, respectively. On the other hand, figures 5–7 were obtained at constant temperature ($T = 0.8$) and scanning the surface field. This set of figures nicely shows that the critical behaviour can be captured using both scaling fields, either the temperature or the surface field.

It is found that the total magnetization exhibits a sharp drop close to the size dependent precursor of the critical point, which becomes clearer when increasing the lattice size (figures 2 and 5). It is worth mentioning that all curves have a common intersection point, which follows

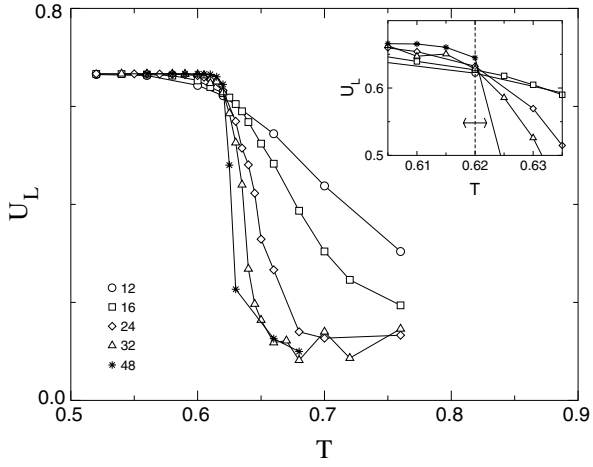

Figure 4. Plots of the fourth order cumulant versus T as obtained keeping $h_1 = 0.6$ constant and using lattices of different sizes as shown in the figure. The inset shows a detailed view of the intersection point of the curves corresponding to samples of different sizes. The double arrow gives an estimate of the error involved in the determination of the intersection point.

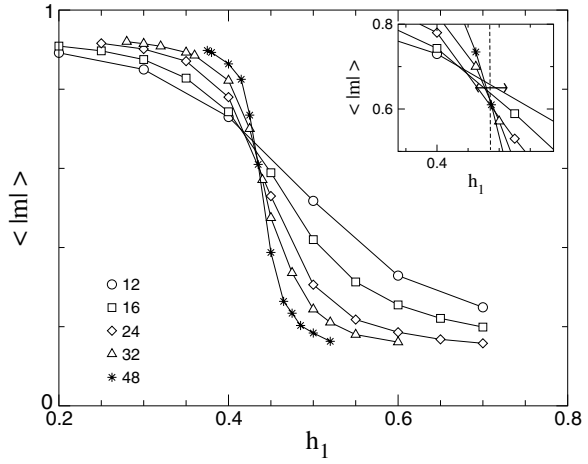

Figure 5. Plots of the magnetization $|m|$ versus h_1 as obtained keeping $T = 0.8$ constant and using lattices of different sizes as shown in the figure. The inset shows a detailed view of the intersection point of the curves corresponding to samples of different sizes. The double arrow gives an additional estimate of the error involved in the determination of the intersection point.

from the fact that the magnetization of the film scales as

$$m = \frac{m_s}{L} = \frac{\xi_\parallel^{1/2}}{L}\tilde{m}_s(L\xi_\parallel^{-1/2}, L^2\xi_\parallel^{-1}, h\xi_\parallel^{3/2}) \tag{33}$$

cf equation (11) for $M \sim L^2$. Since at T_w we have $\xi_\parallel \sim L^2$, it follows that all moments of $P(m)$ are simply functions of $L^2\xi_\parallel^{-1}$ only,

$$\langle |m|^k \rangle = \tilde{m}_k(L^2\xi_\parallel^{-1}). \tag{34}$$

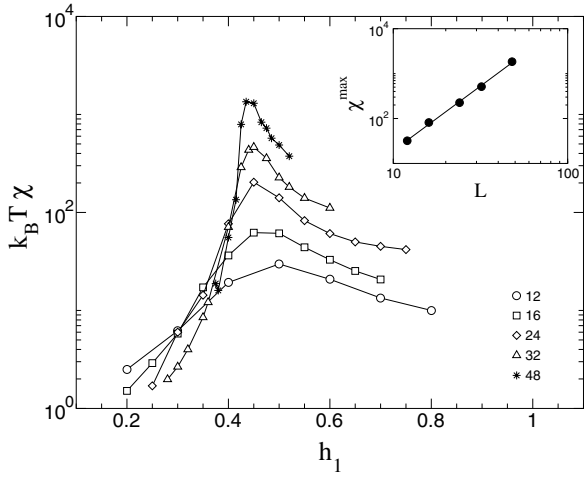

Figure 6. Plots of the susceptibility versus h_1 as obtained keeping $T = 0.8$ constant and using lattices of different sizes as shown in the figure. The inset shows the size dependence of the maximum of the susceptibility $k_B T \chi^{max}$. The straight line shows the fit $\chi^{max} \sim L^3$.

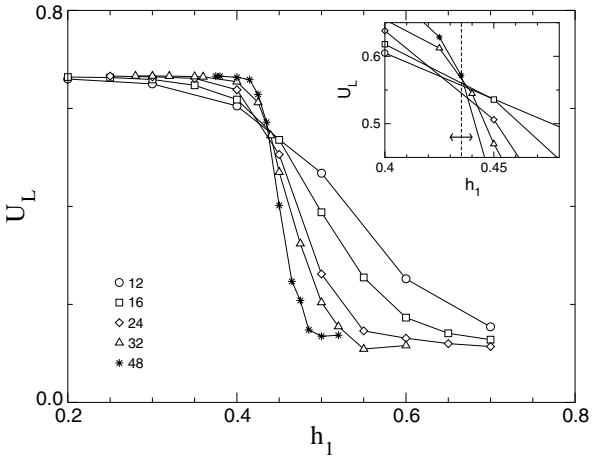

Figure 7. Plots of the fourth order cumulant versus h_1 as obtained keeping $T = 0.8$ constant and using lattices of different sizes as shown in the figure. The inset shows a detailed view of the intersection point of the curves corresponding to samples of different sizes. The double arrow gives an estimate of the error involved in the determination of the intersection point.

This follows readily from $\langle l \rangle \sim \xi_\perp$. The intersection point is used as an additional estimation of the critical point.

The cumulants also exhibit the expected behaviour. In fact, for both $T \ll T_c$ (figure 4) and $h_1 \ll h_{1c}$ (figure 7) one has $U_L \to 2/3$, while far above the critical point U_L tends to vanish. In spite of the statistical scattering of the data observed above criticality, it is still possible to identify the intersection point of the curves corresponding to samples of different sizes (see the insets of figures 4 and 7) and consequently to obtain an additional estimate of the critical point.

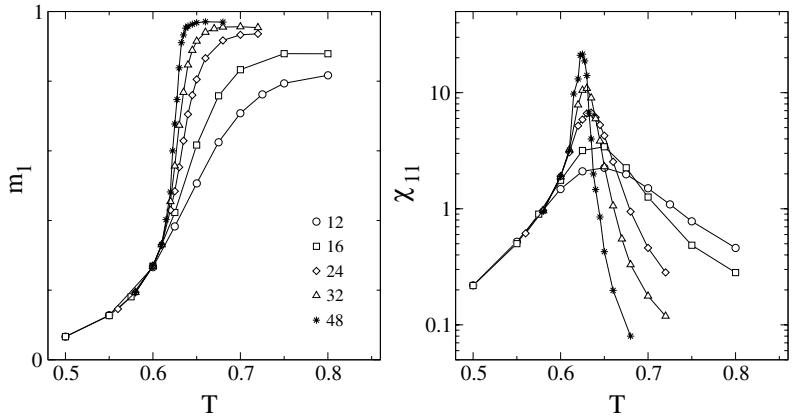

Figure 8. Plots of the surface layer magnetization m_1 and susceptibility χ_{11} as a function of the temperature, for $h_1 = 0.6$ and different lattice sizes as indicated.

On the other hand the susceptibility exhibits the typical single-peaked shape. These peaks are rounded and shifted due to finite-size effects (figures 3 and 6). The insets in these figures show the dependence of the maximum value of the susceptibility ($\chi^{\max}$) on the lattice width L. In both cases the dependence $\chi^{\max} \sim L^3$ holds, as in the case of short-range fields [10].

Besides the estimates for the critical points based on the intersection points of both the magnetization and the cumulant, it is also possible to obtain an additional value using data of the susceptibility. In fact, defining the size dependent critical temperature (field) $T_c(L)$ ($h_{1c}(L)$) as the position of the peak of the susceptibility, an extrapolation to the thermodynamic limit $L \to \infty$ can be performed by using equation (10).

Furthermore, figure 8 shows the variation of the surface quantities m_1 and χ_{11} with the temperature, for a surface field $h_1 = 0.6$. While m_1 behaves smoothly and hence is not very suitable to accurately locate the interface transition, the surface susceptibility χ_{11} shows a sharp peak which can be used as a reliable estimation of $T_c(L)$.

Figures 9 and 10 summarize the obtained results for the location of the finite size critical points. The extrapolated critical points unfortunately show only rough agreement with our previous estimates based on the magnetization and the cumulant, as also shown in the figures. Probably, the linear dimensions $L = 12$–48 are not large enough for the asymptotic laws of equation (10) to hold. Thus, we rely on the estimates based on cumulant intersection in the following.

Based on the obtained values for the critical points we have drawn the wetting phase diagram, as shown in figure 11. Let us recall that the extreme cases of the diagram are known exactly, namely $h_1(0) = [\sum_{n=1}^{\infty} n^{-3}]^{-1}$ [31], while for $T = T_{c,b}$ one has $h_1 = 0$. Also for the sake of comparison we have included the critical curve corresponding to the Ising model with short-range surface fields that has been solved exactly [40].

3.3. The localization–delocalization transition of the interface.

After drawing the wetting phase diagram we have performed simulations aimed to study the critical behaviour of the interface. To this purpose it is essential to have an efficient algorithm capable to accurately locate the interface. Therefore let us first briefly outline the standard method [56] used in order to evaluate the local position of the interface, $\ell(x)$. For each column

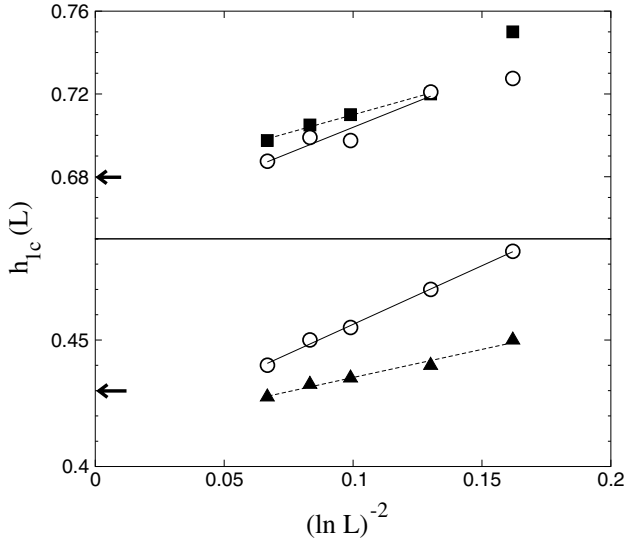

Figure 9. Plots of $h_{1c}(L)$ versus $(\ln L)^{-2}$ as obtained for $T = 0.5$ (top panel) and $T = 0.8$ (lower panel). Circles indicate data extracted from the maximum of the susceptibility, while squares and triangles are data extracted from the distribution $P(m_0)$ and the surface susceptibility χ_{11}, respectively. The fit according to equation (10) (see the lines) allows us to extrapolate to the thermodynamic limit and to obtain $h_{1w}(T)$. Independent estimates of the critical fields obtained from both the magnetization and the cumulant are also shown for the sake of comparison (see the arrows).

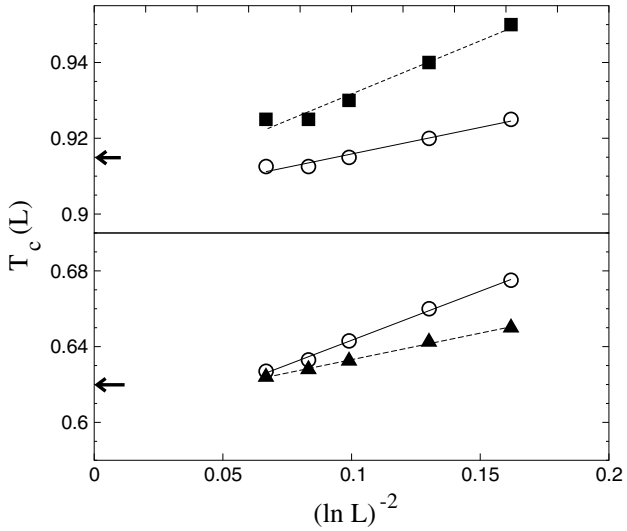

Figure 10. Plots of $T_c(L)$ versus $(\ln L)^{-2}$ as obtained for $h_1 = 0.25$ (top panel) and $h_1 = 0.6$ (lower panel). Circles indicate data extracted from the maximum of the susceptibility, while squares and triangles are data extracted from the distribution $P(m_0)$ and the surface susceptibility χ_{11}, respectively. The fit according to equation (10) (see the lines) allows us to extrapolate to the thermodynamic limit and to obtain $T_w(h_1)$. Independent estimates of the critical temperatures obtained from both the magnetization and the cumulant are also shown for the sake of comparison (see the arrows).

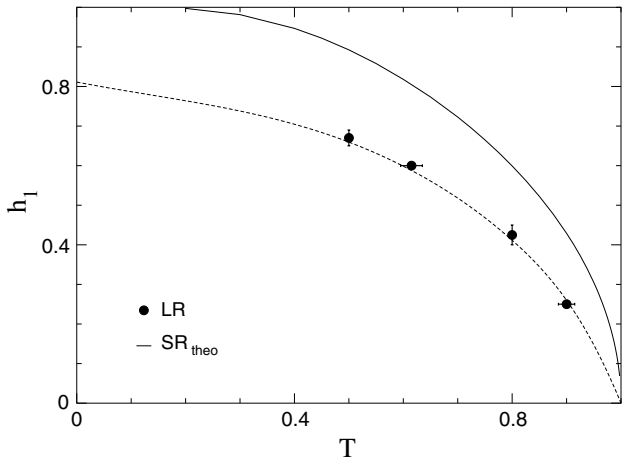

Figure 11. Wetting phase diagram for the Ising model with surface fields of long range (LR) of the form $h(z) \sim h_1/z^3$. Circles are Monte Carlo results obtained by means of extrapolations to the thermodynamic limit. The dashed line has been drawn to guide the eyes taking into account that the extreme points for $T = 0$ and $T_{c,b}$ are known exactly. The exact solution [40] for the critical curve corresponding to short-range (SR) fields, given by equation (3), is also shown for the sake of comparison (full line).

i one has to evaluate the summation given by

$$v(\ell) = \sum_{j=1}^{L} [S(i, j) - p(j - \ell)]^2, \tag{35}$$

where $p(z)$ is a step function such as $p = 1$ for $z < 0$ and $p = -1$ for $z > 0$. The value of ℓ that minimizes the summation is then defined as the position of the interface at the ith column. Using this procedure, the function $\ell(x)$, that assumes integer values between zero and L for the range $1 \leqslant x \leqslant M$, is obtained. Figure 12 shows a set of snapshots of typical spin configurations together with the corresponding interface configuration, as obtained by use of this algorithm. These data correspond to a fixed surface field $h_1 = 0.6$ and several temperatures, for a lattice of thickness $L = 48$. One can observe that, for low T ($T = 0.61$, $T = 0.62 < T_c(L) \approx 0.625$), the interface remains bound to one wall as expected for the non-wet phase. Increasing T ($T = 0.625, 0.6275$), the detachment of the interface from the wall and the subsequent excursions can be observed. Finally, for $T > T_c(L)$ the interface is found running along the centre of the film as expected for the wet phase.

After using the method described above for the location of the interface, it is possible to compute the distribution function $P(\ell)$, that gives the probability of finding the interface at the position $\ell(x)$ along the strip.

Figure 13 shows plots of $P(\ell)$ and $m(z)$ obtained using a lattice of size $L = 48$, keeping $h_1 = 0.6$ constant and changing the temperature. It is found that for $T < T_c(L)$ the interface becomes *localized* close to the walls, where the distribution exhibits two symmetric peaks. This behaviour is in qualitative agreement with the observed snapshots and corresponds to the non-wet regime. Note that in the case of a first-order interface localization–delocalization transition (which would also be compatible with the finite size analysis presented above) we would expect to see three distinct peaks of $P(\ell)$ in the transition region, separated by deep minima from each other. This is not the case here. On approaching the critical temperature, it is expected that the mean position of the interface $\langle \ell \rangle$ should diverge exponentially according

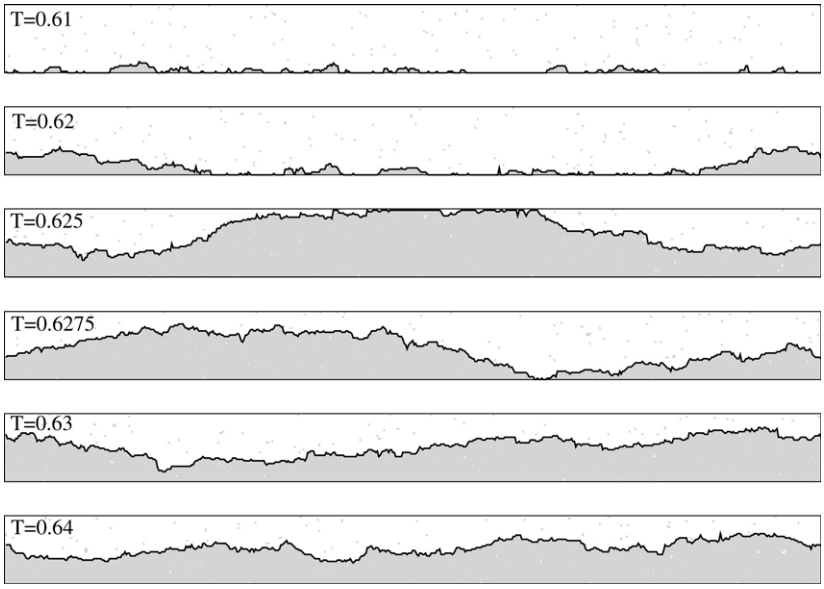

Figure 12. Snapshots of the Ising film for $L = 48$, $M = 576$, $h_1 = 0.6$ and different temperatures as indicated. Spins $S_i = +1$ are shown in black, and spins $S_i = -1$ are not shown. The configuration of the interface is indicated by a thick line.

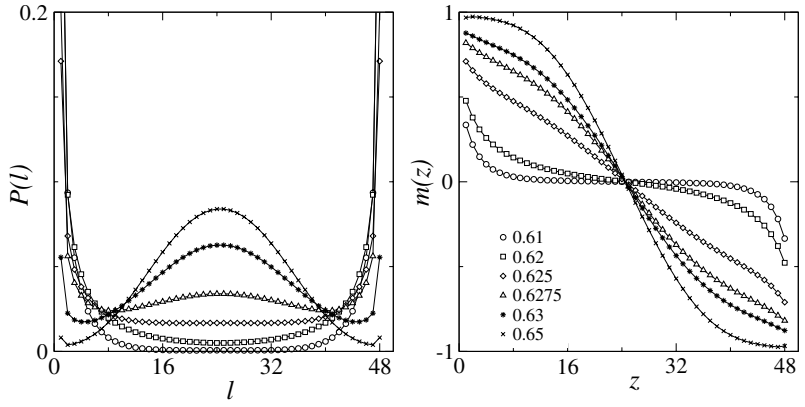

Figure 13. Plots of the probability distribution $P(\ell)$ for the position of the interface (left panel) and the magnetization profiles $m(z)$ across the film (right panel), obtained for $h_1 = 0.6$ and changing the temperature around the critical one given by $T_c(L) = 0.625$. It should be noticed that due to the fact that $h_L \equiv -h_1 P(\ell)$ is symmetric and $m(z)$ is antisymmetric with respect to the centre of the film, $z = L/2$.

to $\langle \ell \rangle \sim \exp(h_{1c} - h_1)^{-1/2}$ (see equation (6) and figure 14). Of course, for a finite strip of thickness L, such a divergence is actually limited by $L/2$.

Just at the wetting critical point, $P(\ell)$ should be a flat line with an average height of $1/L$, so that the interface is truly delocalized and can be found, with the same probability, at any position along the strip. However, this behaviour is hard to observe in our simulations since the transition to the wet phase is quite abrupt. By increasing the temperature one reaches

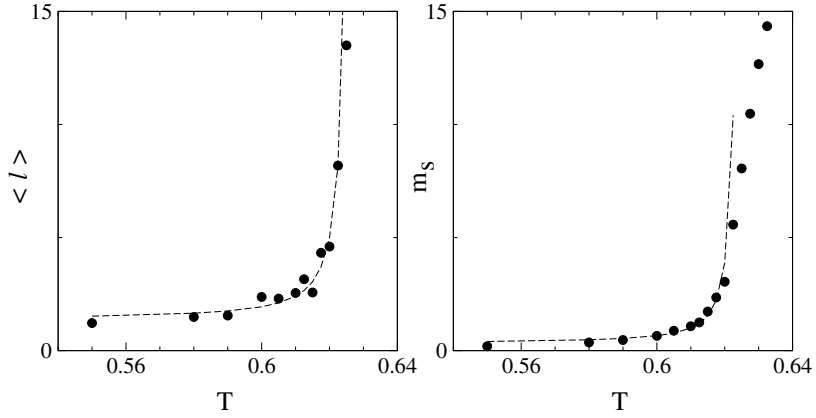

Figure 14. Plots of the mean position of the interface ($\langle \ell \rangle$) and the surface excess magnetization m_s versus the temperature, as obtained for $h_1 = 0.6$ and using a lattice of size $L = 48$. The lines are fits of the data to an exponential dependence given by equation (6).

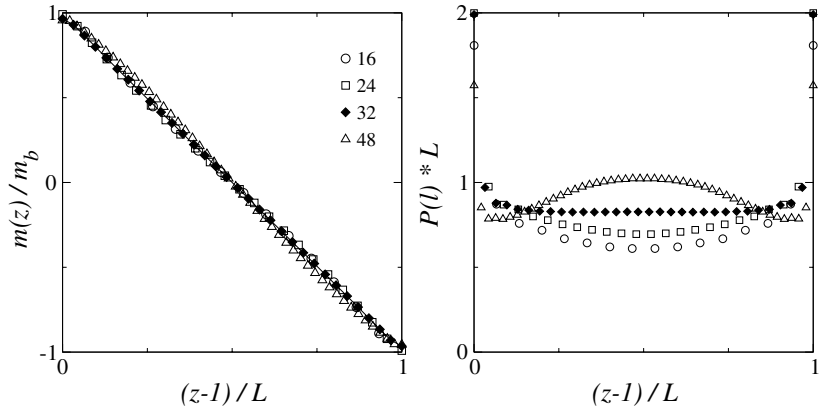

Figure 15. Plots of the magnetization profiles $m(z)$ across the film (left panel) and the probability distribution $P(\ell)$ for the position of the interface (right panel), for different lattice sizes as indicated. The temperature is $T = 0.8$ and the surface field $h_1 = 0.45$.

the wet phase for $T > T_c$ and now the competing effect of the surface fields causes $P(\ell)$ to develop a single peak at the centre of the strip $z = L/2$. The properties of the *delocalized* interface within this wet regime are analysed in section 3.5. In a similar way, upon raising the temperature at fixed field the magnetization profiles show the behaviour already observed for the interface transition with short-range boundary fields [9–11]. They remain nearly flat in the middle of the film for $T < T_c$, become almost linear around T_c, and then adopt a typical sigmoidal shape in the wet phase ($T > T_c$). Using these profiles and equation (32) we have also calculated the surface excess magnetization m_s (see figure 14), which plays the same role as the mean position of the interface $\langle \ell \rangle$. The observed exponential divergence confirms this picture.

The behaviour of the magnetization profiles close to the critical point provides evidence of the subtle role played by the finite size effects. In fact, figure 15(a) shows that the profiles measured at $T = 0.8$ and $h_1 = 0.45$ are almost linear with systematic deviations. The best

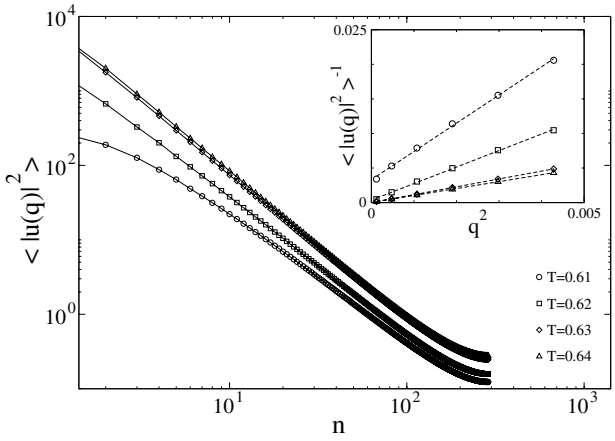

Figure 16. Plots of the Fourier spectra $\langle |u(q)|^2 \rangle$ of the position of the interface $\ell(x)$, for $h_1 = 0.6$ and different temperatures as indicated. The inset shows the linear fitting devoted to estimating the correlation length $\xi_\parallel$ and the interface stiffness $\beta\Gamma$. The integer index n runs from 1 to M and $q \equiv (2\pi/M)n$.

linear profile corresponds to $L = 32$ and for this lattice size it can also be observed that the distribution function of the interface is almost flat. These results are in agreement with the fact that $h_1 = 0.45$ is the effective critical field for $L = 32$, as shown already in the extrapolations of figure 9. For $h_1 = 0.45$ the lattice of size $L = 48$ is above its critical point ($h_1 \approx 0.44$) so that this lattice is slightly within the wet phase. Therefore, the profile tends to deviate towards a sigmoidal shape (figure 15(a)) while $P(\ell)$ exhibits a smooth peak around the centre of the sample (figure 15(b)). For the smaller lattices with $L = 16$ and 24 the value $h_1 = 0.45$ effectively lies within the non-wet phase and then the distribution of the interface has a minimum at the centre of the film, while the magnetization profiles look slightly flattened in the middle.

It is also of interest to analyse the behaviour of the correlation lengths close to the transition, as done in previous simulation studies of the case of short-range surface fields [33]. To this purpose we have also evaluated the Fourier spectrum of the interface function $\ell(x)$, see figure 16. After fitting the data to the theoretical expectation (cf equation (18)), as shown in the inset of figure 16, we are able to estimate the dependence of $\xi_\parallel$ on both T and L.

The dependence of the length scales $\xi_\parallel$ and $\xi_\perp$ on the film thickness L is described in figure 17. Very close to the wetting critical point ($T = 0.8$, $h_1 = 0.45$) the relationship $\xi_\parallel \sim L^2$ holds in agreement with theoretical predictions (see equation (20)). Furthermore, the evaluation of the fluctuations of the interface position allows us to estimate the interfacial width s. Figure 17 then also shows a linear dependence of the type $\xi_\perp^2 \sim s^2 \sim L^2$, as expected from equation (25).

On the other hand, figure 18 presents the dependence of both correlation lengths on the temperature, for a sample of size $L = 48$. Figure 18(a) shows that $w \sim \xi_\perp$ diverges exponentially when approaching the critical wetting point, according to equation (6). The best fit of the data gives $\xi_{0\perp}^- \approx 0.3$ and $b_\perp^- \approx 0.25$ for $h_1 < h_{1c}$, while for $h_1 > h_{1c}$ one has $\xi_{0\perp}^+ \approx 5.4$ and $b_\perp^+ \approx 0.1$. Furthermore, as shown in figure 18(b), $\xi_\parallel$ also diverges exponentially at criticality. In this case we have obtained $\xi_{0\parallel}^- \approx 1.5$, $b_\parallel^- \approx 0.5$ ($h_1 < h_{1c}$), and $\xi_{0\parallel}^+ \approx 59.0$, $b_\parallel^+ \approx 0.2$ ($h_1 > h_{1c}$). Results obtained measuring the spin–spin correlation function are also in qualitative agreement with those estimated from the correlations along the interface (figure 18).

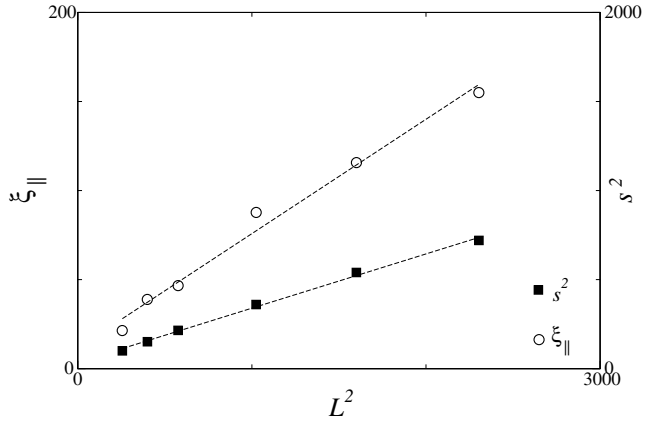

Figure 17. Plots of the correlation length and the width of the interface, as a function of the film thickness L. The temperature is $T = 0.8$ and the surface field is $h_1 = 0.45$.

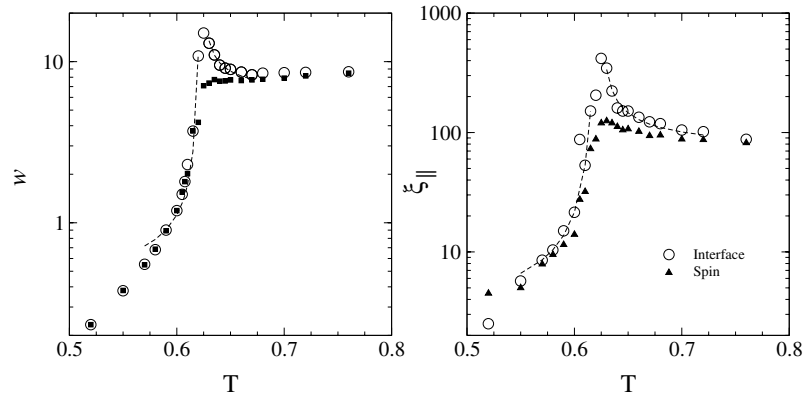

Figure 18. Plots of the width w (left panel) and the correlation length $\xi_\parallel$ (right panel) of the interface, as a function of the temperature at fixed field $h_1 = 0.6$. The lattice size is $L = 48$. The width w is obtained from the correlation function $G(\ell(x))$ (circles) and from the magnetization profiles (squares). The length $\xi_\parallel$ is obtained from $G(\ell(x))$ (circles) and from the spin–spin correlation function $G(x, z = L/2)$ (triangles). Dashed lines correspond to fits according to equation (6).

By using the data shown in figure 18 we are able to check the relationship between the length scales $\xi_\parallel$ and $\xi_\perp$. In fact, plots of $\xi_\parallel$ versus w^2 ($\xi_\perp^2$) for values of T close to the critical one are found to be linear above and below the critical point (see figure 19). This confirms that, despite the fact that both exponents $\nu_\parallel$ and $\nu_\perp$ are infinite, the relationship $\nu_\parallel = 2\nu_\perp$ still holds for long-range surface fields as used in the present work.

3.4. Influence of the bulk magnetic field

In order to further clarify the critical behaviour of the interface we have also addressed the case of complete wetting, i.e. we considered the dependence on the bulk magnetic field $h < 0$ at a fixed temperature T and fixed surface field $h_1 \geqslant h_{1c}(T)$. Figure 20 shows the results for the choice $T = 0.8$ and $h_1 = 0.435$, which corresponds to one of the extrapolated critical points. From the probability distribution $P(\ell)$ and the magnetization profiles $m(z)$ we extract

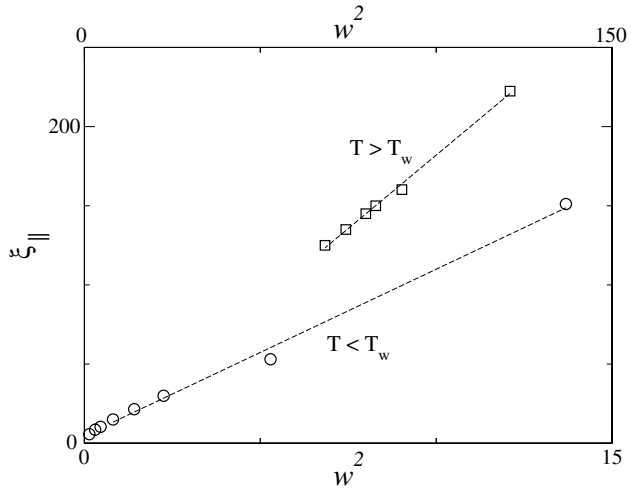

Figure 19. Plots of the correlation length versus the width of the interface. Data are taken from figure 18. The bottom (upper) x-scale corresponds to $T < T_w$ ($T > T_w$).

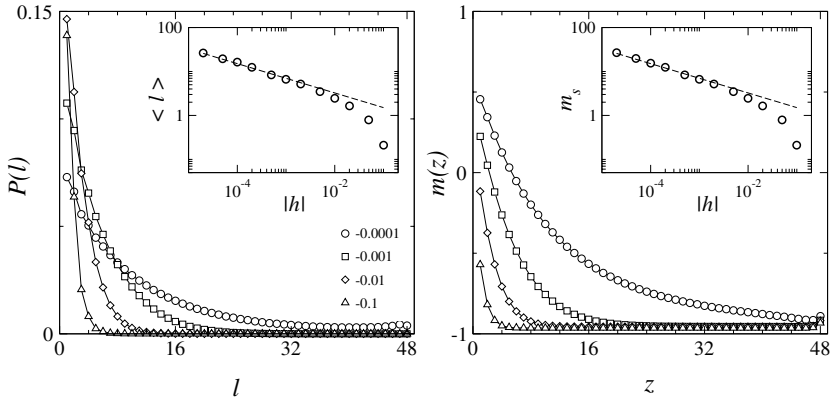

Figure 20. Plots of the probability distribution $P(\ell)$ for the position of the interface (left panel) and the magnetization profiles $m(z)$ across the film (right panel), for different values of the bulk magnetic field h as indicated. The temperature $T = 0.8$ and the surface field $h_1 = h_{1c} = 0.435$ are constant. The insets show the mean position of the interface $\langle \ell \rangle$ and the excess magnetization m_s respectively. The dashed lines correspond to a power law with exponent $\beta^{co} = 1/3$.

the (equivalent) lengths $\langle \ell \rangle$ and m_s, respectively. One can observe the power law divergence of both quantities, with the predicted theoretical value $\beta^{co} = 1/3$ (see equations (7) and (12)).

Additionally, after evaluating the Fourier spectra of the interface and using equation (18), we have determined the dependence of both the stiffness $\beta\Gamma$ and $\xi_\parallel$ on the bulk field, as shown in figure 21. The observed increase of the interfacial stiffness with $|h|$ can be assigned to the constraining effect of the field, that shifts the mean position of the interface towards the wall. In this way the wandering of the interface becomes more restricted. The predicted relationship $\xi_\parallel \sim |h|^{-\nu_\parallel^{co}}$ with $\nu_\parallel^{co} = 2/3$ (see equation (7)) is observed for $|h| > 10^{-4}$, while for weaker fields $\xi_\parallel$ tends to the equilibrium value already determined for $h \equiv 0$; see e.g. figure 18.

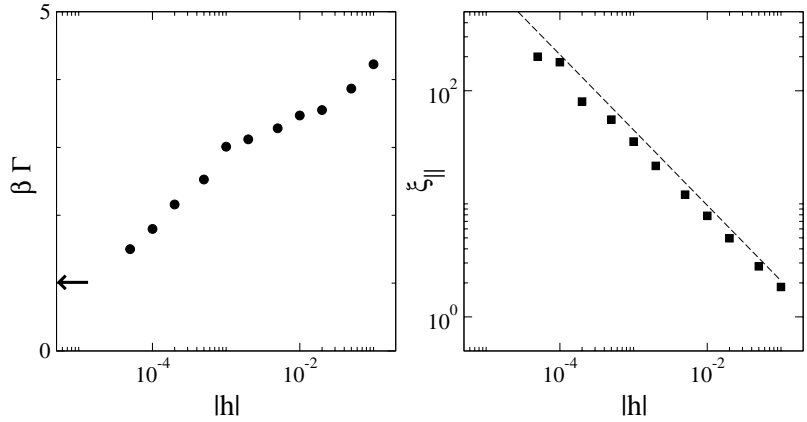

Figure 21. Plots of the effective stiffness $\beta\Gamma$ (left panel) and the parallel correlation length $\xi_\parallel$ (right panel), as a function of the bulk magnetic field h. The surface field $h_1 = 0.6$ and the temperature $T = T_c(h_1) = 0.625$ are constant. The arrow in the left panel indicates the exact value of $\beta\Gamma$ in the asymptotic limit $|h| = 0$. The dashed line in the right panel corresponds to a power law with exponent $\nu_\parallel^{co} = 2/3$.

3.5. Study of the delocalized interface.

Within the wet phase, namely for $T_w(h_1) < T < T_{c,b}$, interfaces become delocalized and some of their relevant properties can be studied by means of measurements of the magnetization profiles and the distribution function of the interface position.

Figure 22(a) shows plots of the magnetization profiles ($m(u = z - L/2)$) that have been used to evaluate the *effective* width of the interface (w) by fitting the curves to an error function,

$$m(z) \equiv \frac{1}{M}\sum_{x=1}^{M} S(x,z) = -m_0 \,\mathrm{erf}\left(\frac{\sqrt{\pi}(z - L/2)}{2w}\right), \tag{36}$$

where the constant m_0 is of the order of the bulk magnetization.

On the other hand, the *effective* profile can be obtained from the convolution of the *intrinsic* profile and the distribution of the local position of the interface ($P(u)$, see figure 22(b)). The intrinsic profile is given by

$$m^{(i)}(z) = -m_0 \,\mathrm{erf}\left(\frac{\sqrt{\pi}(z - L/2)}{2w_0}\right), \tag{37}$$

where the *intrinsic* width w_0 accounts for the internal structure of the interface. Also the distribution $P(u)$ describing the fluctuations in the local position of the interface is expected to be a Gaussian according to the theory of capillary waves, so one has

$$P(u) = \frac{1}{\sqrt{2\pi s^2}} \exp\left(-\frac{u^2}{2s^2}\right), \tag{38}$$

where $u(x) \equiv \ell - L/2$, and the width of the capillary waves s^2 is evaluated by using equation (22). Therefore, performing the convolution, the effective profile becomes

$$m^{(a)}(z) = \int_{-\infty}^{\infty} \mathrm{d}u\, m^{(i)}(z - u) P(u). \tag{39}$$

Inserting equations (37) and (38) into equation (39) we obtain

$$w^2 = w_0^2 + \frac{\pi}{2} s^2. \tag{40}$$

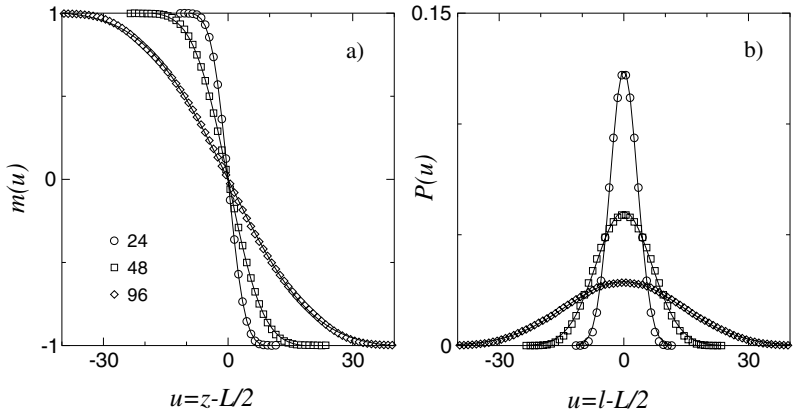

Figure 22. (a) Plots of the magnetization profiles $m(u)$ as a function of $u = z - L/2$. Data obtained by taking $T = 0.50$, $h_1 = 1.0$ and using lattices of different sizes, as listed in the figure. Full lines correspond to the fits of the data to the *error* function (see equation (36)). (b) Plots of the distribution $P(u)$ as a function of $u = \ell - L/2$, as obtained for the same set of parameters as in (a). The full lines are obtained after fitting the data to a Gaussian function (see equation (38)).

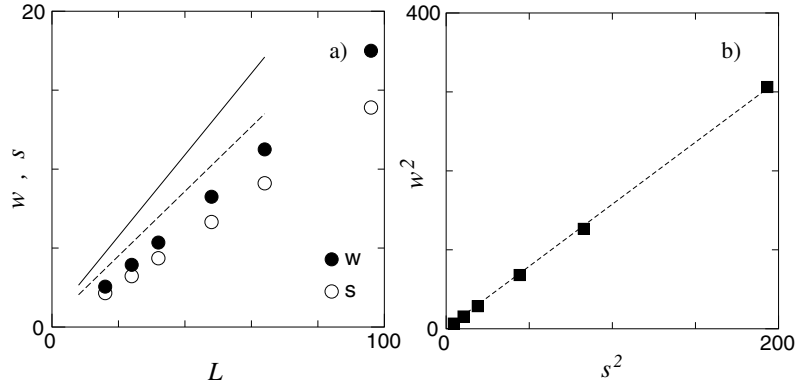

Figure 23. (a) Plots of the effective width (w) and the width of the fluctuations (s) versus the film thickness L. Data are taken from the fits shown in figures 22(a) and (b), respectively. For the sake of comparison, the full (dashed) line shows the dependence of w (s) which is obtained simulating the confined Ising strip with short-range surface fields. (b) Plot of w^2 versus s^2. The dashed line shows the function $w^2 = w_0^2 + \pi/2 s^2$, where $w_0 = 0.706$ corresponds to the intrinsic width of an Ising interface [41] (see equation (40)).

Equation (40) provides a relationship between the quadratic intrinsic width and two quantities that can be measured by means of numerical simulations: the width of the capillary waves and the width of the magnetization profiles.

Figure 23(a) shows a plot of the effective width, as obtained by fitting the magnetization profiles shown in figure 22(a) by means of equation (36), versus the lattice size L. Also the width of the capillary waves as obtained after fitting the curves shown in figure 22(b) with the aid of equation (38) is shown in figure 23(a).

The plots in figure 23(a) confirm the linear dependence of w and s on the lattice width L, as predicted by both the theory of capillary waves ($s \sim L$, see equation (20)) and the transfer matrix method applied to films with short-range fields (equation (21)). For the sake of

comparison, figure 23(a) also includes our results for the case of short-range fields. It becomes evident that the long-range nature of the fields tends to stabilize the fluctuations of the position of the interface by restricting the magnitude of its width, as expected.

Next, by using the values of w and s already measured we are able to test the validity of equation (40). This is shown in figure 23(b). It follows that the linear relationship, with slope $\pi/2$ and constant $w_0 = 0.706$ [41], holds quite well.

3.6. The correlation length and the surface tension

For the semi-infinite Ising strip, the correlation length $\xi_\parallel$ describes the asymptotic decay of the correlation function along the centre of the film,

$$G(x', z = L/2) \equiv \langle S(x, z)S(x + x', z)\rangle \sim \exp(-x'/\xi_\parallel). \tag{41}$$

In the simulations one actually calculates the correlation function along the centre of the film, while fitting equation (41) with an exponential decay the correlation length $\xi_\parallel$ can be obtained.

On the other hand, the theory of capillary waves provides a useful relationship between the Fourier spectrum of local fluctuations ($u(q)$) the correlation length $\xi_\parallel$ and the effective surface stiffness $\beta\Gamma$, given by equation (18). So, one has two methods to evaluate the correlation length and the results may provide a stringent test of the theory.

Let us now derive the relationship between the correlation length $\xi_\parallel$ and the width L of the sample in view of the interplay between short- and long-range effects.

The energy of the interface influenced by a long-range (LR) surface field can be accounted for by an effective potential $V_{\rm LR}(\ell)$, given by

$$V_{\rm LR}(\ell) = \int_0^L {\rm d}z\, h(z)m(z) \tag{42}$$

where $h(z)$ is given by equation (2). Also, the magnetization profile is roughly approximated by a step function $m(z) = \Theta(\ell - z) - \Theta(z - \ell)$, such that

$$m(z) = \begin{cases} +1 & \text{if } z < \ell \\ 0 & \text{if } z = \ell \\ -1 & \text{if } z > \ell. \end{cases}$$

Now solving equation (42), performing a double derivative with respect to ℓ and evaluating it at the centre of the film, one has

$$|V''_{\rm LR}(u = 0)| = 12h_1 L^{-4}, \tag{43}$$

that combined with equation (19) from the capillary wave theory gives the following relationship for the correlation length:

$$\xi_{\parallel{\rm LR}} = \sqrt{\frac{\Gamma L^4}{12h_1}}, \tag{44}$$

that increases with the second power of the film width L, as in the case of short-range fields. In order to compare the prediction of equation (44) with the simulation results we have taken $\Gamma = 2.2$ for $T = 0.5$ [19].

On the other hand, short-range (SR) surface fields also influence the magnetization profiles close to the walls, and such a disturbance decays exponentially towards the centre of the film. In this way, an effective wall–interface interaction is also present for SR fields. According to transfer matrix calculations [19, 58], this interaction leads to the following dependence of $\xi_{\parallel{\rm SR}}$

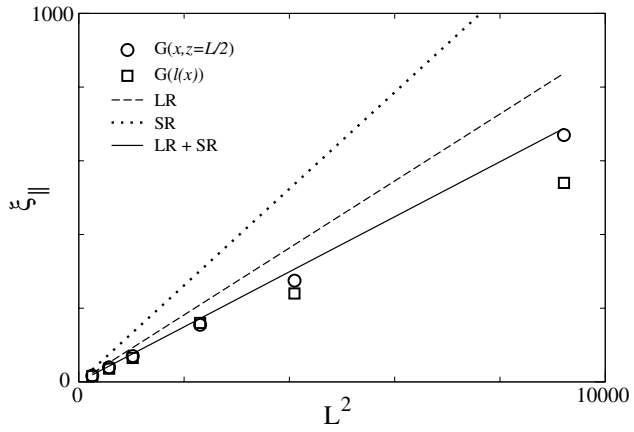

Figure 24. Plots of the correlation length $\xi_{\parallel}$ versus L^2. Results obtained from the spectra of the fluctuations of the interface according to equation (18) (squares), and from the spin correlation function along the centre of the film (circles). The dotted (dashed) line corresponds to the contribution of SR (LR) fields as follows from equation (45) ((44)). The full line accounts for both SR and LR contributions, according to equation (46).

on L (see also equation (21)):

$$\xi_{\parallel \mathrm{SR}} = \frac{2\beta\Gamma}{3\pi^2} L^2. \tag{45}$$

Now we assume that the influence of both short- and long-range interactions has to be considered to give the total contribution to the correlation length. Therefore, according to equation (19) the summation has to be performed as follows:

$$\xi_{\parallel}^{-2} \approx \xi_{\parallel \mathrm{SR}}^{-2} + \xi_{\parallel \mathrm{LR}}^{-2}. \tag{46}$$

Figure 24 shows a comparison between the theoretical calculations and the simulation results obtained by using two different methods: the fit of the correlation function $G(x, z = L/2)$ according to equation (41) and the evaluation of the Fourier spectra (see equation (18)). As follows from figure 24, simulation results corresponding to both evaluation methods are in excellent agreement for small values of L, but an observable systematic discrepancy emerges when L is increased. It also follows that both long (LR) and short-range (SR) contributions overestimate the values for the correlation length, while the interplay between SR and LR effects, as evaluated according to equation (46), provides the best description of the numerical data.

On the other hand, with the aid of the Fourier spectra of the fluctuations of the interface (equation (18)) it is possible to evaluate the dependence of the effective surface stiffness $\beta\Gamma$ on the film thickness L, as shown in figure 25. Since the correlation length $\xi_{\parallel}$ increases when increasing the thickness of the film, the stiffness decreases approaching the value of the free interface given by $\beta\Gamma = 1.9394$ [19]. This behaviour has already been observed in the case of short-range surface fields, which is also shown in figure 25 for the sake of comparison. Also the dependence $\beta\Gamma \sim L^{-2}$, as predicted theoretically [16], is observed.

4. Conclusions

In this paper we have presented detailed Monte Carlo simulations of Ising films in two dimensions, where competing surface fields which decay as a power law with the distance to the

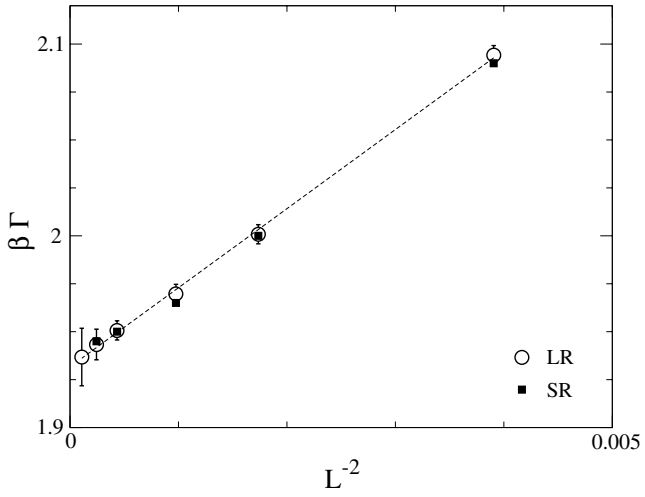

Figure 25. Plot of the effective stiffness $\beta\Gamma$ versus the film thickness L, as obtained from the spectra of the fluctuations of the interface. The dashed line is a fit to the expected theoretical decay proportional to L^{-2}. Results corresponding to short-ranged fields are also shown for the sake of comparison. Notice that in both cases the asymptotic value for $L \to \infty$ is given by $\beta\Gamma = 1.9394$, which corresponds to the free interface.

wall are applied. The specific system studied here, with surface fields of the type $h(z) \sim h_1/z^3$, is interesting for several reasons. First, it displays a localization–delocalization transition of the interface which belongs to an unusual universality class. Theoretical calculations based on effective Hamiltonian models predicts that upon varying the temperature (or the equivalent scaling field h_1) across the transition the relevant length scales diverge exponentially instead of in the usual power law fashion [62, 64]. This behaviour could be clearly observed in our simulations, where the divergence of both parallel and perpendicular correlation lengths was determined by means of several defined quantities.

Besides this, the location of the critical line for this transition, in the (T, h_1) plane is not known exactly to date. In this sense this paper makes a contribution, by presenting a comprehensive numerical study of the finite size effects for this transition. By using the cumulant intersection method we extract estimates for the critical wetting points, and the phase diagram is then drawn with the addition of two other points which are previously known. After the write-up of our paper was essentially completed, we learned about an independent study (A Drzewiński and K Szola, preprint entitled 'Corrections to the Kelvin equation for long-range boundary fields') obtaining this wetting phase diagram by means of numerical density matrix renormalization group techniques. Using systems $L \times \infty$ with L up to $L = 690$, the approach to the thermodynamic limit could be studied reliably in this work. Gratifyingly, the resulting wetting phase diagram is in very good agreement with our estimation in figure 11. Interestingly, this work does not obtain any evidence of a $(\ln L)^{-2}$ law for finite-size shifts, raising doubts about the corresponding suggestion of [31] (equation (10) of the present paper).

The observed dependence of the correlation lengths on the film thickness is well described by current theories [55].

Once the critical curve had been obtained, we focused on the influence of a bulk (uniform) magnetic field on the critical behaviour of the films. This corresponds to the case of complete wetting, and we were able to observe the predicted power law divergence of the correlation length.

Then we addressed the study of the properties of the delocalized interface. The effective width as measured by the magnetization profiles and the capillary wave contribution were related through a convolution approximation, which reproduces very well the data if an intrinsic width corresponding to Ising interfaces [41] is assumed. Furthermore, a small decrease of the interfacial width was observed, as compared to the case of short-range wall fields. This effect has also been observed in computer simulation studies of polymer models [59].

We believe these results are of the interest due to the lack of a exact solution for the model under study.

Acknowledgments

The authors would like to thank A Maciolek for useful discussions. This work is supported financially by CONICET, UNLP and ANPCyT (Argentina). EVA acknowledges the Alexander von Humboldt Foundation (Germany) for a fellowship. ADV acknowledges DAAD (Germany) for a scholarship.

References

[1] de Gennes P G 1985 *Rev. Mod. Phys.* **57** 827
[2] Sullivan D E and Telo da Gama M M 1986 *Fluid and Interfacial Phenomena* ed ed C A Croxton (New York: Wiley)
[3] Dietrich S 1988 *Phase Transitions and Critical Phenomena* vol 12, ed C Domb and J L Lebowitz (London: Academic)
[4] Schick M 1990 *Liquids at Interfaces* ed J Charvolin *et al* (Holland: Elsevier)
[5] Forgacs G, Lipowsky R and Nieuwenhuizen Th M 1991 *Phase Transitions and Critical Phenomena* vol 14, ed C Domb and J L Lebowitz (London: Academic)
[6] Parry A O 1996 *J. Phys.: Condens. Matter* **8** 10761
[7] Fisher M E and Nakanishi H 1981 *J. Chem. Phys.* **75** 5857
[8] Nakanishi H and Fisher M E 1983 *J. Chem. Phys.* **78** 3279
[9] Albano E V, Binder K, Heermann D and Paul W 1989 *Surf. Sci.* **223** 151
[10] Albano E V, Binder K, Heermann D and Paul W 1989 *Z. Phys.* B **77** 445
[11] Albano E V, Binder K, Heermann D and Paul W 1990 *J. Stat. Phys.* **61** 161
[12] Parry A O and Evans R 1990 *Phys. Rev. Lett.* **64** 439
[13] Swift M R, Owczarek A L and Indekeu J O 1991 *Europhys. Lett.* **14** 465
[14] Gradmann U 1991 *J. Magn. Magn. Mater.* **100** 481
[15] Binder K and Landau D P 1992 *J. Chem. Phys.* **96** 1444
[16] Parry A O and Evans R 1992 *Physica* A **181** 250
[17] Binder K, Landau D P and Ferrenberg A M 1995 *Phys. Rev. Lett.* **74** 298
Binder K, Landau D P and Ferrenberg A M 1995 *Phys. Rev.* E **51** 2823
[18] Binder K, Landau D P and Ferrenberg A M 1995 *Phys. Rev.* E **53** 5023
[19] Maciolek A and Stecki J 1996 *Phys. Rev.* B **54** 1128
[20] Maciolek A 1996 *J. Phys. A: Math. Gen.* **29** 3837
[21] Werner A, Schmid F, Müller M and Binder K 1997 *J. Chem. Phys.* **107** 8175
[22] Karevski D and Henkel M 1997 *Phys. Rev.* B **55** 6429
[23] Carlon E and Drzewiński A 1998 *Phys. Rev.* E **57** 2626
[24] Carlon E, Drzewiński A and Rogiers J 1998 *Phys. Rev.* B **58** 5070
[25] Ferrenberg A M, Landau D P and Binder K 1998 *Phys. Rev.* E **58** 3353
[26] Liu H, Bhattacharya A and Chakrabarti A 1998 *J. Chem. Phys.* **109** 8607
[27] Aign T *et al* 1998 *Phys. Rev. Lett.* **81** 5656
[28] Frisch H L, Puri S and Nielaba P 1999 *J. Chem. Phys.* **110** 10514
[29] Slen J, Swan A K and Wendelken J F 1999 *Appl. Phys. Lett.* **75** 2987
[30] Tsay J-S and Yao Y-D 1999 *Appl. Phys. Lett.* **74** 1311
[31] Albano E V, Binder K and Paul W 2000 *J. Phys.: Condens. Matter* **12** 2701
[32] Müller M, Albano E V and Binder K 2000 *Phys. Rev.* E **62** 5281
[33] De Virgiliis A, Albano E V, Müller M and Binder K 2005 *Physica* A **352** 477

[34] Binder K 1983 *Phase Transitions and Critical Phenomena* vol 8, ed C Domb and J L Lebowitz (New York: Academic)
[35] Iglói F and Indekeu I O 1990 *Phys. Rev.* B **41** 6836
[36] Ebner C, Hayot F and Cai J 1990 *Phys. Rev.* B **42** 8187
[37] Le Bouar Y, Loiseau A, Finel A and Ducastelle F 2000 *Phys. Rev.* B **61** 3317
[38] Ising E 1925 *Z. Phys.* **31** 253
[39] McCoy B M and Wu T T 1973 *The Two Dimensional Ising Model* (Cambridge, MA: Harvard University Press)
[40] Abraham D B 1980 *Phys. Rev. Lett.* **44** 1165
[41] Abraham D B 1981 *Phys. Rev. Lett.* **47** 545
[42] Binder K and Hohenberg P C 1972 *Phys. Rev.* B **6** 3461
[43] Au-Yang H and Fisher M E 1975 *Phys. Rev.* B **11** 3469
[44] Fisher M E and DeGennes P G 1978 *C. R. Acad. Sci. Paris* **287** 207
[45] Fisher M E and Au-Yang H 1980 *Physica* A **101** 255
[46] Au-Yang H and Fisher M E 1980 *Phys. Rev.* B **21** 3956
[47] Abraham D B and Issyeoni M E 1980 *J. Phys. A: Math. Gen.* **13** L89
[48] Nicolaides D B and Evans R 1989 *Phys. Rev.* B **9** 9336
[49] Albano E V, Binder K, Heermann D and Paul W 1989 *J. Chem. Phys.* **91** 3700
[50] Stecki J, Maciolek A and Olausen K 1994 *Phys. Rev.* B **49** 1092
[51] Stecki J 1993 *Phys. Rev.* B **47** 7519
[52] Onsager L 1944 *Phys. Rev.* **65** 117
[53] Privman V and Švrakić N M 1988 *Phys. Rev.* B **37** 3713
[54] Binder K, Evans R, Landau D P and Ferrenberg A M 1996 *Phys. Rev.* E **53** 5023
[55] Privman V 1992 *Int. J. Mod. Phys.* C **3** 857
[56] Müller M and Schick M 1996 *J. Chem. Phys.* **105** 8885
[57] Lipowsky R 1984 *Phys. Rev. Lett.* **52** 1429
Lipowsky R 1991 *Phys. Rev. Lett.* **67** 2987
[58] Abraham D B and Švrakić N M 1986 *Phys. Rev. Lett.* **56** 1172
[59] Werner A, Müller M, Schmid F and Binder K 1999 *J. Chem. Phys.* **110** 1221
[60] Kosterlitz J M and Thouless D J 1973 *J. Phys. C: Solid State Phys.* **6** 1181
[61] Binder K 1981 *Z. Phys.* B **43** 119
[62] Kroll D M and Lipowsky R 1983 *Phys. Rev.* B **28** 5273
[63] Kroll D M, Lipowsky R and Zia R K P 1985 *Phys. Rev.* B **32** 1862
[64] Lipowsky R and Nieuwenhuizen T 1988 *J. Phys. A: Math. Gen.* **21** L89
[65] Fisher M E 1984 *J. Stat. Phys.* **34** 667
[66] Fisher M E 1986 *J. Chem. Soc. Faraday Trans.* II **82** 1569
[67] van Leeuwn J and Hilhorst H 1981 *Physica* A **107** 319
[68] Chui S and Weeks J 1981 *Phys. Rev.* B **23** 2438
[69] Burkhardt T 1981 *J. Phys. A: Math. Gen.* **14** L63